A&A manuscript no.
(will be inserted by hand later)

Your thesaurus codes are:
06.01.3, 06.03.1, 06.07.2, 06.15.1, 06.16.2

ASTRONOMY
AND
ASTROPHYSICS
24.1.1998

Small-scale topology of solar atmosphere dynamics

II. Granulation, K2v grains and waves

N.M. Hoekzema and R.J. Rutten

Sterrekundig Instituut, Postbus 80000, NL–3508 TA Utrecht, The Netherlands

Accepted August 12 1997

Abstract. We continue studying the small-scale topology of dynamical phenomena in the quiet-sun internetwork atmosphere through statistical estimation of the co-location probability of different fine-structure elements and wave modes. In this paper we chart spatial alignments between the granular brightness structuring of the photosphere, Ca II K_{2V} brightness patterns in the chromosphere, and wave amplitude patterns in both regimes as a function of time delay between the occurrences of the various features. These charts confirm the presence of excess 2–4 min waves above dark intergranular lanes, the absence of excess 5 min waves above bright granules, the absence of expected alignments between photospheric and chromospheric wave patterning, and the broad-band nature of Ca II K_{2V} grain formation. In addition, they show significant alignments at large time delays that seem to be regulated by mesoscale patterning and pattern migration.

Key words: Sun: atmosphere – Sun: photosphere – Sun: chromosphere – Sun: granulation – Sun: oscillations

1. Introduction

This is the second of two papers analysing cospatial filtergram sequences of the solar photosphere and chromosphere taken with the Swedish Vacuum Solar Telescope on La Palma. Our goal is to search for local relations between waves and fine structure in the quiet photosphere and the overlying chromosphere.

The first paper (Hoekzema et al. 1997; henceforth Paper I) described the science context, the data, the reduction procedures and initial results from wave-amplitude correlations between the photosphere (as imaged in the Fraunhofer G band, called G below) and the chromosphere (Ca II K_{2V} filtergrams, called K below). Its main conclusion was that at small spatial scales global and local modulation combine into a complex mix which betrays signatures of local wave excitation by intergranular lanes and displays persistent mesoscale patterning in the chromosphere. The latter may arise from subsurface wave sources and subsurface diffraction. In this paper we extend the analysis by studying such wave and fine structure relations in time-lapse fashion, searching for spatial alignments of different dynamical patterns admitting time delays between them.

The data and the approach are the same as in Paper I. We again combine the Fourier amplitude maps constructed in Paper I with the statistical correspondence factor C introduced there to search for spatial alignments between wave patterning at various periodicities in the photosphere and the chromosphere and the brightness patterning of the photospheric granulation. In this paper we permit considerable time delay between the various waves and features and add the chromospheric internetwork brightness patterning in order to study the occurrence of the so-called Ca II K_{2V} grains. The latter form a topic of much debate. It has been reviewed by Rutten & Uitenbroek (1991) and Rutten (1994, 1995, 1996); a summary of pertinent new work is given in Paper I. In brief, the internetwork K_{2V} grains portray an acoustic shock phenomenon (Carlsson & Stein 1997), but the nature of the underlying pistons and their patterning remain open issues.

In summary, the small-scale topology patterns addressed here consist of photospheric and chromospheric spatial wave amplitude distributions at 5-min periodicity (photospheric p-modes), 3-min periodicity (chromospheric oscillation) and 2-min periodicity (propagating acoustic waves) and of photospheric and chromospheric brightness patterning (granulation and K_{2V} grains). Our searches first chart the time-lapse co-alignment between the brightness structures (Figs. 1–3), then between the various types of waves (Fig. 4), and finally between waves and brightness structures (Figs. 5–6). We again limit the searches to

Send offprint requests to: R.J. Rutten

the internetwork regions in our field of view in order to restrict the analysis to non-fluxtube dynamics.

In the next section we summarize the data, the construction of the Fourier maps and the definition of the correspondence factor given in Paper I, and we define the additional brightness classifications used here. The results are given in Sect. 3 and discussed in Sect. 4. The various time-delay correspondence charts provide intriguing hints of piston properties and piston persistence which again point to the importance of mesoscale patterning in the dynamical coupling between the photosphere and the internetwork chromosphere.

2. Data, reduction, analysis

Our input data consist of a double sequence of co-temporal and co-spatial images of the photosphere (G band, called G below) and the overlying chromosphere (Ca II K_{2V}, called K below). The two sequences consist of 228 processed images at 20 s cadence covering a quiet-sun field of 29×25 Mm^2 (41×36 arc sec^2). Examples are shown in Fig. 2 of Paper I.

The two sequences were split in ten partially overlapping 22-min segments. Each was apodized to an effective duration of about 15 min to produce pixel-by-pixel Fourier amplitude maps at different periodicities. This short duration was selected to provide Fourier diagnostics, in particular separation of 5-min and 3-min wave modes, per location with classification as to granular morphology. Examples of the resulting Fourier maps are shown in Fig. 6 of Paper I; they provide the input material for the wave pattern analyses in Figs. 4–6 below. The total 75-min sequence of overlapping segments permits to study temporal evolution and time-delayed co-alignments of the different Fourier maps. Their partial independence also provides root-mean-square error estimates.

As in Paper I, we divide the brightness patterns and the Fourier amplitudes in different classes to which a given pixel of the observed field may belong. The G pixels are again split, per locally-normalized 15-min average, into granules and lanes (above and below average brightness, respectively). "Bright granules" again denote the subset with brightness over 110% of the average value, "dark granules" the subset below 90%.

The K pixels are again split into network and internetwork as specified in Fig. 3 of Paper I. All figures below employ internetwork pixels exclusively. In addition, we now introduce "bright K" and "dark K" pixels, where the bright ones are the internetwork pixels in a K filtergram with brightness over 130% of the mean internetwork value, the dark ones those below 70%. They describe the extrema of the spidery internetwork pattern seen on the K filtergram movie; their filling factors are about 9% and 18% of the internetwork, respectively. The bright K pixels represent a good proxy for the K_{2V} grains observed on Ca II K line-core spectrograms, as demonstrated by the spatio-temporal bandwidth comparisons in Fig. 2 of Rutten (1994). A somewhat different definition is used for Fig. 6 below.

The Fourier amplitudes are again split between above and below average. In addition, we now use extreme "large A" regions with Fourier amplitude A over twice the map average and "low A" regions with amplitude less than half the average. Their filling factors are 4–6% and 18–20%, respectively.

Finally, all figures below use the spatial correspondence parameter $C = f_{\rm AB}/f_{\rm B}$ defined at the end of Sect. 3 in Paper I. The coincidence filling factor $f_{\rm AB} = N_{\rm AB}/N_{\rm A}$ specifies the fraction of pixels of type A in the internetwork region of one map that also belong to type B in another map. The filling factor $f_{\rm B} = N_{\rm B}/N$ measures the spatial occurrence of the second category in the internetwork. With this normalization the spatial correspondence C quantifies the likelihood that the two types of behavior are cospatial in terms of the random-draw likelihood, so that $C = 1$ suggests that A and B are independent phenomena, values $C > 1$ imply that pixels of type A are preferentially co-located with pixels of type B, values $C < 1$ imply spatial avoidance. Let us clarify its usage by adding an example to those in Paper I. Of all pixels that are designated "bright K" in the internetwork parts of a K image, 10% shows up as a "bright granule" at the corresponding location in the concurrent 15-min G average. Since the bright granules cover only 8% of the internetwork area, the spatial correspondence at $\Delta t = 0$ between bright K pixels and bright granules is $C \approx 0.10/0.08 = 1.3$. It expresses that bright K occurrence favors co-location with bright granules in G by 30% over the random-draw probability. This statistical probability may be estimated reliably from large data sets even for pixel classes with small filling factor and in the presence of multiple patterning agents. It does not depend on the amplitude of each signal, only its spatial distribution.

3. Results

3.1. Photospheric brightness

Figure 1 displays time-delay correspondence between granular features. The various curves in the upper panel quantify the temporal alignment of granules with granules, lanes with lanes, and granules with lanes. The lower panel does the same for bright granules and dark lanes. The time resolution is 20 s. The sampling varies between 227 C values at $\Delta t = 20$ s and 48 C values at $\Delta t = 60$ min, so that the rms variations increase towards the right.

The curves show high correspondence (avoidance for cross-alignment) up to $\Delta t \approx 10$ min, making that value a granular lifetime estimate. All curves reach $C \approx 1$ at $\Delta t = 17$ min with the exception of the dark-lane curve (thin solid) in the lower panel. This value would represent the maximum lifetime of granular features if the curves

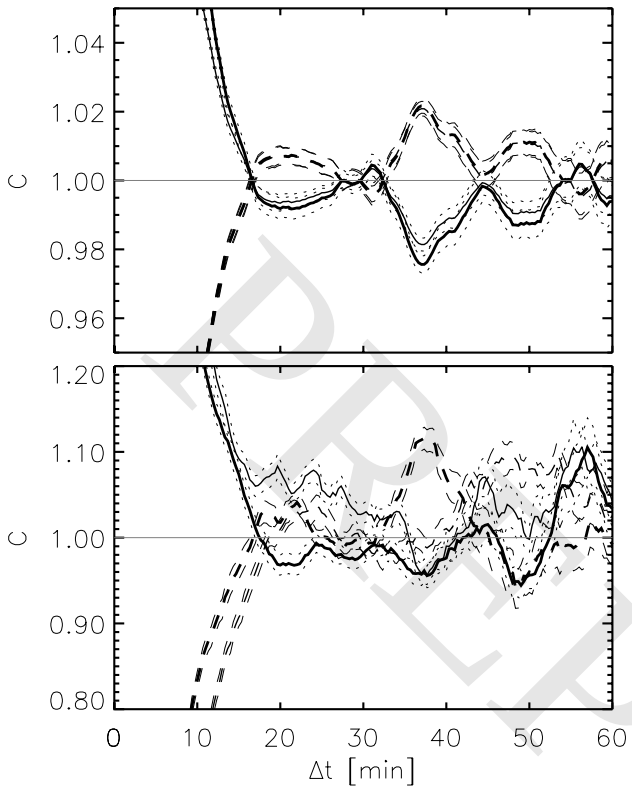

Fig. 1. Persistence of granules and intergranular lanes, measured as spatial correspondence C between various G brightness classes as function of elapsed time Δt. The value $C = 1$ implies absence of spatial alignment, $C > 1$ preferential co-location, $C < 1$ spatial avoidance. The upper panel is for granules and lanes, the lower panel for the extreme subclasses made up by bright granules and dark lanes (see text). Thick solid curves: spatial correspondence between pixels belonging to granules and pixels that belong to granules Δt later (upper panel), and similarly for bright granules (lower panel). Thin solid curves: similarly between lanes and subsequent lanes (upper panel) and between dark lanes and subsequent dark lanes (lower panel). Thick dashed curves: similarly between lanes and granules (upper panel) or dark lanes and bright granules (lower panel), with the lanes observed before the granules. Thin dashed curves: similarly but with the granules observed before the lanes. One-sigma error estimates are added to each curve (dotted or dashed)

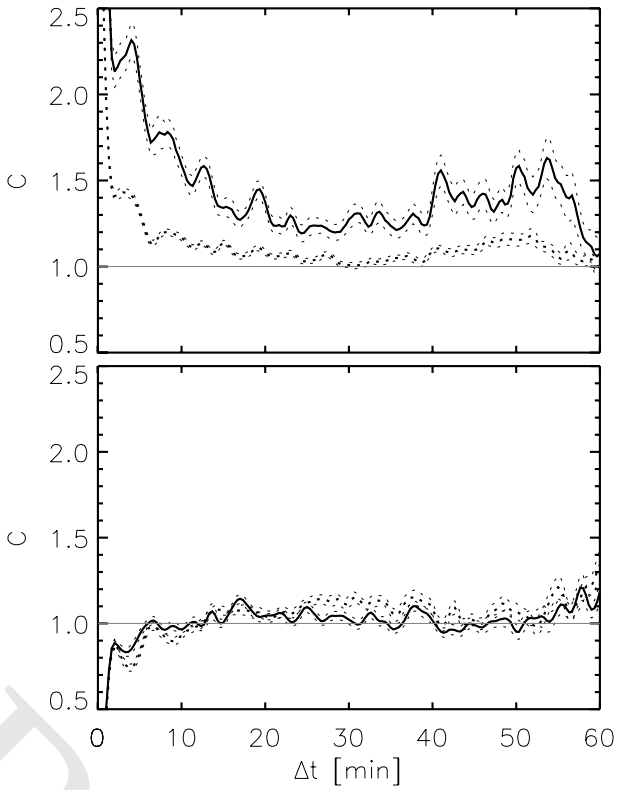

Fig. 2. Ca II K brightness persistence, measured as spatial correspondence C between two K brightness classes as function of elapsed time Δt. The upper panel shows the persistence of bright K pixels (solid curve) and of dark K pixels (dashed curve). The lower panel measures the time-delay correspondence between bright K pixels and dark K pixels, with the solid curve for sampling bright after dark and the dashed curve for sampling dark after bright

would remain flat for longer Δt. They don't; instead, they display significant subsequent modulation. The solid and dashed curves in the upper panel show reverse behavior because the filling factors of granules and lanes are about equal (47% and 53% respectively).

The modulation indicates repetitive recurrence over extended duration. We have checked it by performing tests on another granulation sequence which covers a substantially larger field of view and which will be analysed in a forthcoming paper. It produces similar modulation, but only for small subfields; the modulation amplitude diminishes when the correspondence factor is determined over larger areas. We therefore suspect that the modulation results from the mesoscale flows present in the photosphere (e.g., November et al. 1981; November & Simon 1988; Simon et al. 1988; Title et al. 1989; Brandt et al. 1991; Muller et al. 1992; November 1994; Brandt et al. 1994; Wang et al. 1995). The flow cells measure about 4–8 arcsec and the flow speeds are of the order of 0.5 km s^{-1}. Since our internetwork area samples only a few mesogranular cells (Fig. 1 of Paper I), pattern migration effects are not averaged out in our data. The modulation may therefore represent simple shifts of the granular brightness pattern over granules and lanes.

The larger-field test also reproduces the slow decay for dark lanes in the bottom panel of Fig. 1, indicating that these extreme features tend to persist longer than other granular structures and also tend to maintain their location better (cf. Roudier et al. 1997).

3.2. Chromospheric brightness

Figure 2 is similar to Fig. 1 but concerns the chromospheric K brightness extremes. The bright K pixels show a time-lapse co-alignment probability that remains significantly above a random draw (upper curve in the upper panel). For example, the value $C \approx 1.5$ for the bright K pixels at $\Delta t = 10$ min corresponds to 13.5% of the pixels being bright at both times, whereas only 9% would be bright in a random selection. This preferential co-alignment is larger for the bright K pixels than for the dark K pixels, especially at first. In addition, the curve shows short-period repetition. A Fourier decomposition (not shown) has a strong peak centered at $f = 5$ mHz (3–4 min periodicity). It undoubtedly corresponds to the similar repetition rate seen in K_{2V} grain "trains", for example the one present at $t = 49 - 54$ min in the righthand panel of Fig. 2 of Lites et al. (1993). The steep initial dip displays the characteristic grain lifetime of about a minute; the slow decay over the first 15 minutes shows that grains have slowly decreasing reappearance probability.

The lower panel of Fig. 2 tests whether bright K and dark K pixels are sequentially co-located. Values $C > 1$ in this cross-correspondence plot would imply that bright and dark K pixels prefer to occupy the same locations in succession. Such co-location is not significantly present.

3.3. Chromospheric versus photospheric brightness

The amount of crosstalk between the photospheric and chromospheric brightness features is measured in Fig. 3. The curves in the upper panel describe the spatial correspondence between bright K pixels and the granular structure in the underlying photosphere. The curves in the lower panel do the same for the dark K pixels. The time delay Δt is plotted on a bilogarithmic scale in order to expand the center part which shows intricate structure. At $\Delta t = 0$ bright K pixels have nearly 30% excess probability to lie above a bright granule (thin solid curve in the upper panel), with corresponding avoidance of dark lanes (thin dashed curve) and comparable behavior above granules and lanes (at lower C because these have larger filling factor). The dark K pixels in the lower panel display opposite behavior.

The curves reverse sign rapidly for increasing Δt so that bright K pixels occur preferentially above dark lanes instead of bright granules already after $\Delta t = 2.5$ min. On the other side (negative Δt) the decay is much more gradual. The dip at $\Delta t = 2.5$ corresponds to a similar co-location correlation in Fig. 15 of Rutten (1995) between Ca II H_{2V} grains, measured as a narrow-band phenomenon in high-resolution spectra, and intergranular lanes in the underlying photosphere a few minutes earlier. This correlation suggests a relationship between excess wave excitation in lanes and K_{2V} grain formation after the wave travel time to the overlying chromosphere. We return to this scenario in Sect. 4.

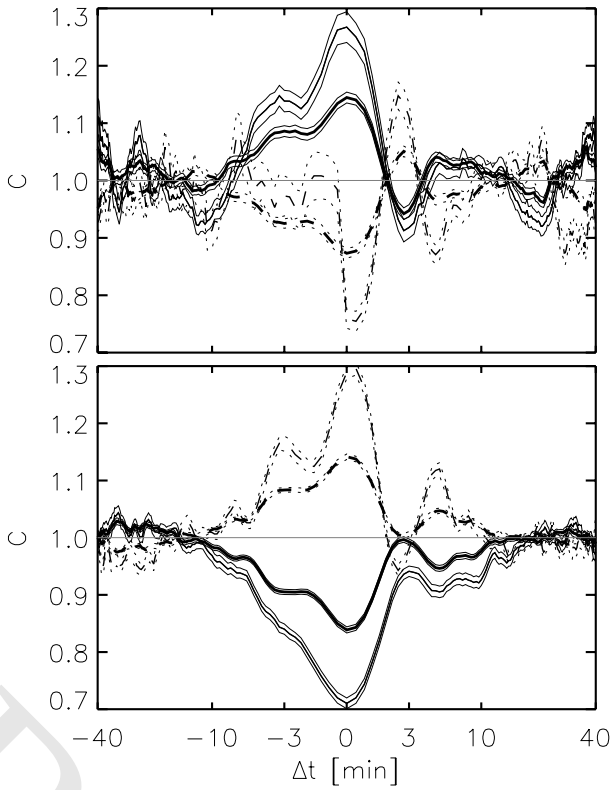

Fig. 3. Crosstalk between chromospheric internetwork intensity contrast and photospheric granulation, measured as spatial correspondence C between various G and K brightness classes as function of elapsed time Δt. The upper panel is for bright K pixels, the lower panel for dark K pixels. Thick solid curves: bright or dark K pixels measured Δt after granules. Thin solid: bright or dark K measured Δt after bright granules. Thick dashed: bright or dark K measured Δt after lanes. Thin dashed: bright or dark K measured Δt after dark lanes

For large Δt, both positive and negative, the curves in Fig. 3 show increasing undulations that resemble the modulation in Fig. 1 and may again be due to mesoscale pattern migration. Their amplitudes are indeed smaller for the dark K pixels (lower panel) which occur twice as frequent as bright K pixels. The dark K curves also show much smaller reversals at $\Delta t = 2.5$ min. This difference with the curves in the upper panel illustrates that bright and dark K pixels do not occur in anti-symmetrical manner, as is also evident when comparing bright and dark K_{2V} behavior in spectral sequences (Cram & Damé 1983; Lites et al. 1993; Hofmann et al. 1996; Carlsson & Stein 1997).

3.4. Waves versus waves

We now turn to the Fourier amplitude maps constructed and displayed in Paper I. Such maps are available for the

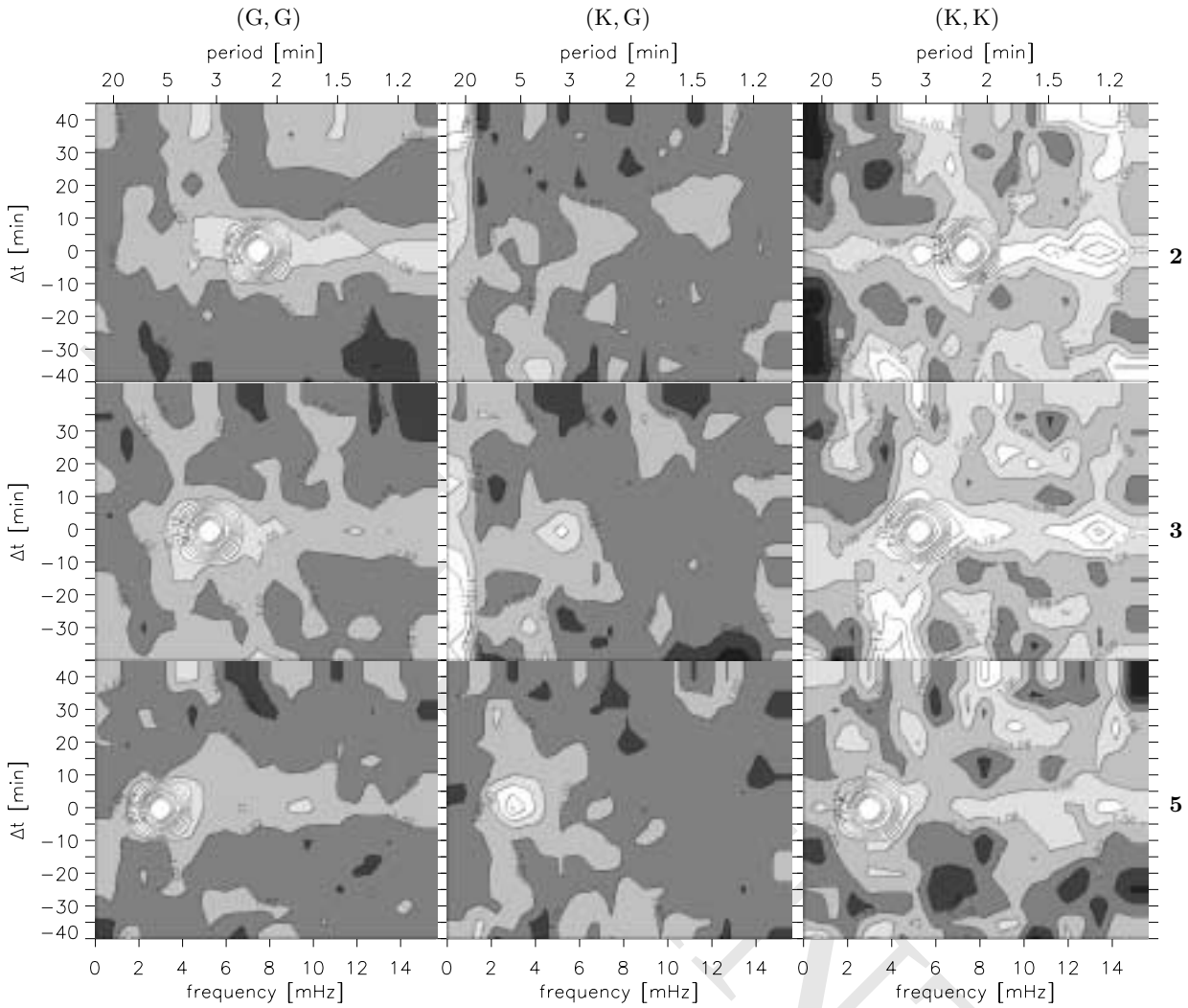

Fig. 4. Time delay charts of the spatial correspondence C between Fourier amplitude maps for the photosphere (G) and the chromosphere (K) in different combinations. The contours specify the value of C between internetwork pixels with larger than average Fourier amplitude in both maps per $(f, \Delta t)$ comparison pair, averaged over the available data segments (ten around $\Delta t = 0$). Grey ($C = 1$) implies absence of spatial correlation, bright ($C > 1$) spatial co-alignment and dark ($C < 1$)) spatial avoidance. The values of C are specified along the contours. Lefthand column: (G,G) = three G amplitude distributions compared with all other G amplitude distributions. Middle column: same for (K,G) pairs. Righthand column: same for (K,K) pairs. Upper row: correspondence between the spatial distribution of Fourier amplitudes in the $f = 7.8$ mHz (2-min periodicity) G or K maps with all other amplitude distributions for G or K. Middle row: same for $f = 5.5$ mHz (3-min). Bottom row: same for $f = 3.1$ mHz (5-min). Horizontal axes: Fourier frequency (bottom) and corresponding periodicity (top). Vertical: time delay Δt between 15-min data segments from which the Fourier maps are constructed, positive when the maps of the given periodicity cover a later 15-min segment than the maps indexed by their frequency along the horizontal axis

full set of frequencies defined by the 22 min segment duration and 20 s image sampling, so that the C measurements between Fourier amplitudes and other patterns may be displayed as two-dimensional charts plotting C as function of both Fourier frequency f and time delay Δt. This is the display format for the remaining figures, with the C values indicated by contours. The split of the data in ten partially independent segments again permits averaging per $(f, \Delta t)$ combination and estimation of the corresponding rms variations. The latter are not shown in these charts but the contour intervals are chosen such that one interval corresponds roughly to one-sigma rms variation or less in the central regions of the charts where ten $(f, \Delta t)$ pairs are averaged.

Figure 4 compares the spatial distributions of the Fourier amplitudes at about 2-min, 3-min and 5-min periodicity in the photosphere (G) and chromosphere (K) with the spatial distributions of all such Fourier maps. The lefthand column charts time-delay Fourier crosstalk between different frequencies in the photosphere, the righthand col-

umn does the same for the chromosphere, and the middle column charts crosstalk between chromosphere and photosphere. The curves in Figs. 9 and 10 of Paper I represent horizontal cuts at $\Delta t = 0$ and vertical cuts at each of the three periodicities through these nine panels.

The (G,G) charts in the lefthand column primarily display self-correspondence in the form of 100% cospatiality peaks around $\Delta t = 0$ at the three periodicities. They reach $C \approx 2$ because the higher-than-average amplitude filling factor is about 50%. The widths of the peaks is set by the frequency and time delay resolutions given by the 22-min (effectively 15-min) segment lengths. There is no outspoken preference for large amplitude to occur or not to occur at the same location at other times or other frequencies, except that there are weak ridges of slight excess co-location at high frequencies around $\Delta t = 0$, especially in the 2-min panel (top). We attribute these ridges to modulation by atmospheric seeing. It jitters small large-contrast features across their actual position and so causes broad-band brightness modulation of which the relative contribution is largest at high frequencies where the intrinsic solar power is smallest (Fig. 4 of paper I).

The (K,K) panels in the righthand column show similar self-correspondence peaks with secondary high-frequency peaks at $\Delta t = 0$ which we again attribute to seeing. The 3-min peak has a tail towards the right. It is also present in the top panel of Fig. 9 in Paper I, where we speculated that shock steepening may produce nonlinear waveforms at this frequency. The whole (K,K) column, especially the 3-min panel, shows a surplus of $C > 1$ values. This indicates that high chromospheric amplitudes tend to be a broad-band phenomenon with relatively long persistence.

The (K,K) charts are very noisy outside the peaks, but a few other features seem significant. There is a patch of white correspondence in the 3–5 min band near the bottom of the 3-min (K,K) panel, suggesting that 3-min waves prefer locations where 4-min waves will occur 20–40 minutes later. The 2-min panel contains a similar patch. The time delay is long enough that this correspondence may again be set by mesoscale pattern migration; we return to this point in Sect. 4.

The 2-min (K,K) chart (top right panel) shows two dark bands along its lefthand side, symmetrically around $\Delta t = 0$, which are the only prominent zones of spatial avoidance in the (K,K) charts. These indicate that locations with above-average 2-min amplitude are preferentially dark well before and well after their 2-min excess. This may similarly point to migration in which internetwork areas that contribute to the self-correspondence peak move out of co-location over this time scale.

The (K,G) charts in the middle column show cross-correspondence peaks between 5-min and 3-min modulation in the chromosphere and the photosphere that are surprisingly low. One would rather expect that both the global p-modes and the local emission of sound waves at or below the surface would produce larger vertical correlation. The low height of these peaks was taken in Paper I (Fig. 9, measured by their $\Delta t = 0$ profile) as evidence of wave diffraction that is caused by subsurface convective inhomogeneities.

The remainder of the (K,G) panels seem without significant structure, except for the extended white blob of $C > 1$ values along the lower left side of the 3-min panel (middle). At $f = 0$ large photospheric amplitude implies the presence of granules, so that this blob suggests that chromospheric 3-min modulation possesses some preferential alignment with locations that subsequently contain granules in the underlying photosphere.

3.5. Photospheric brightness versus waves

The spatial correspondence tests so far have concerned more or less similar quantities, in the form of brightness distributions in Figs. 1–3 and wave amplitude distributions in Fig. 4. We now turn to dissimilar correspondence analysis by studying co-alignments between brightness patterning and wave amplitude patterning, again with two-dimensional charts in the format of Fig. 4. Figure 5 shows such comparison between granular structuring and the wave amplitudes in the photosphere and chromosphere. This is again done for internetwork pixels only and concerns brightness extrema (bright granules and dark lanes only) and wave extrema (over twice and less than half the mean amplitude).

The low-A columns in Fig. 5 differ strikingly from the high-A columns. The first are bland; the second display marked structure. The dark lanes and the bright granules themselves are evident as dark and bright blobs at $\Delta t = 0$ along the lefthand sides of the two high-A G panels because at low frequency the Fourier amplitude describes the average brightness over the 15-min segment duration. The low-A panels show weak reverse contrast along their lefthand sides. For both bright granules and dark lanes, seeing jitter of these small high-contrast structures produces excess power at the highest frequencies (white blobs for $f > 8$ mHz at $\Delta t = 0$ in the high-A G panels).

The dark lanes show large spatial correspondence with high wave amplitudes over the 4–2 min regime (second G panel). This alignment shows fairly large persistence, appreciably longer than the Δt width of the self-correspondence peaks in Fig. 4. The rightmost G panel shows alignment between bright granules and enhanced amplitudes only at $f = 7$ mHz, but avoidance for 3–6 min periodicities which implies that bright granules lack somewhat in high-A 5-min co-location.

The K panels in the upper row are also bland for low wave amplitude. The second panel shows a minor 4-min peak near $\Delta t = 0$ min, adjacent to a zone of avoidance at 3-min periodicity. This steep transition corresponds to the steep drop of the dark-lane curve in the upper panel of Fig. 5 in Paper I, where it was taken to suggest diffrac-

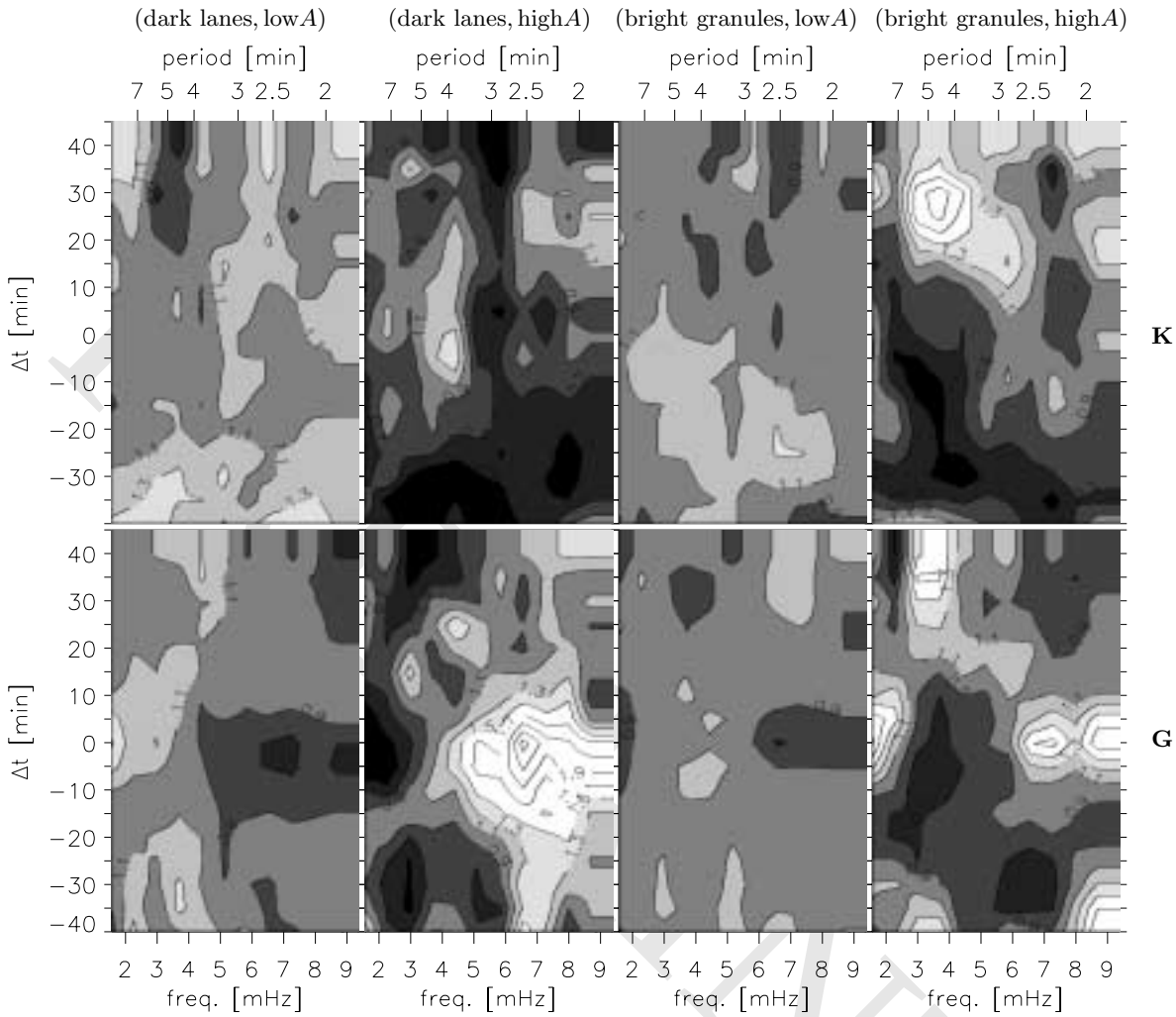

Fig. 5. Time delay charts of the spatial correspondence C between K and G Fourier amplitude and granulation morphology. The format is the same as in Fig. 4, but the contours now specify the amount of alignment between bright granules or dark intergranular lanes in a 15-min averaged G image with the presence of high or low amplitude in K and G Fourier maps for the frequencies specified along the horizontal axis, where high means over twice the average value and low less than half. First column: amount of alignment between dark lanes and low Fourier amplitude. Second column: between dark lanes and high amplitude. Third column: between bright granules and low amplitude. Fourth column: between bright granules and high amplitude. Upper row: K amplitudes (chromosphere). Lower row: G amplitudes (photosphere). Horizontal axes: Fourier frequency (bottom) and periodicity (top). Vertical: time delay Δt between 15-min data segments, positive when the granulation morphology is sampled after the Fourier amplitude

tion of propagating waves ($f > 5$ mHz) away from the lane location over their travel length from photosphere to chromosphere. The large disparity between the second K and G panels indeed indicates that the excess of waves above lanes in the photosphere (lower panel) does not survive as vertical co-location in the overlying chromosphere (upper panel).

The fourth K panel shows a similar avoidance of 5-min enhancement as the corresponding G panel. In addition, it has a significant 4–5 min peak around $\Delta t = 27$ min, implying that bright granules favor locations where the overlying chromosphere showed excess 4–5 min wave amplitudes half an hour earlier. Since it is rather unlikely that chromospheric wave modes control subsurface convection, we again seek the explanation for this delayed correspondence in mesoscale pattern migration (Sect. 4).

3.6. Chromospheric brightness versus waves

Figure 6 is similar to Fig. 5 in that brightness structuring is compared with wave amplitudes, but in this case it is the internetwork K brightness that is tested for spatial correspondence with excesses in the photospheric and chromospheric amplitude distributions. The definition of the bright and dark K pixels is modified from the one used in Figs. 2–3 in that only those pixels that are over

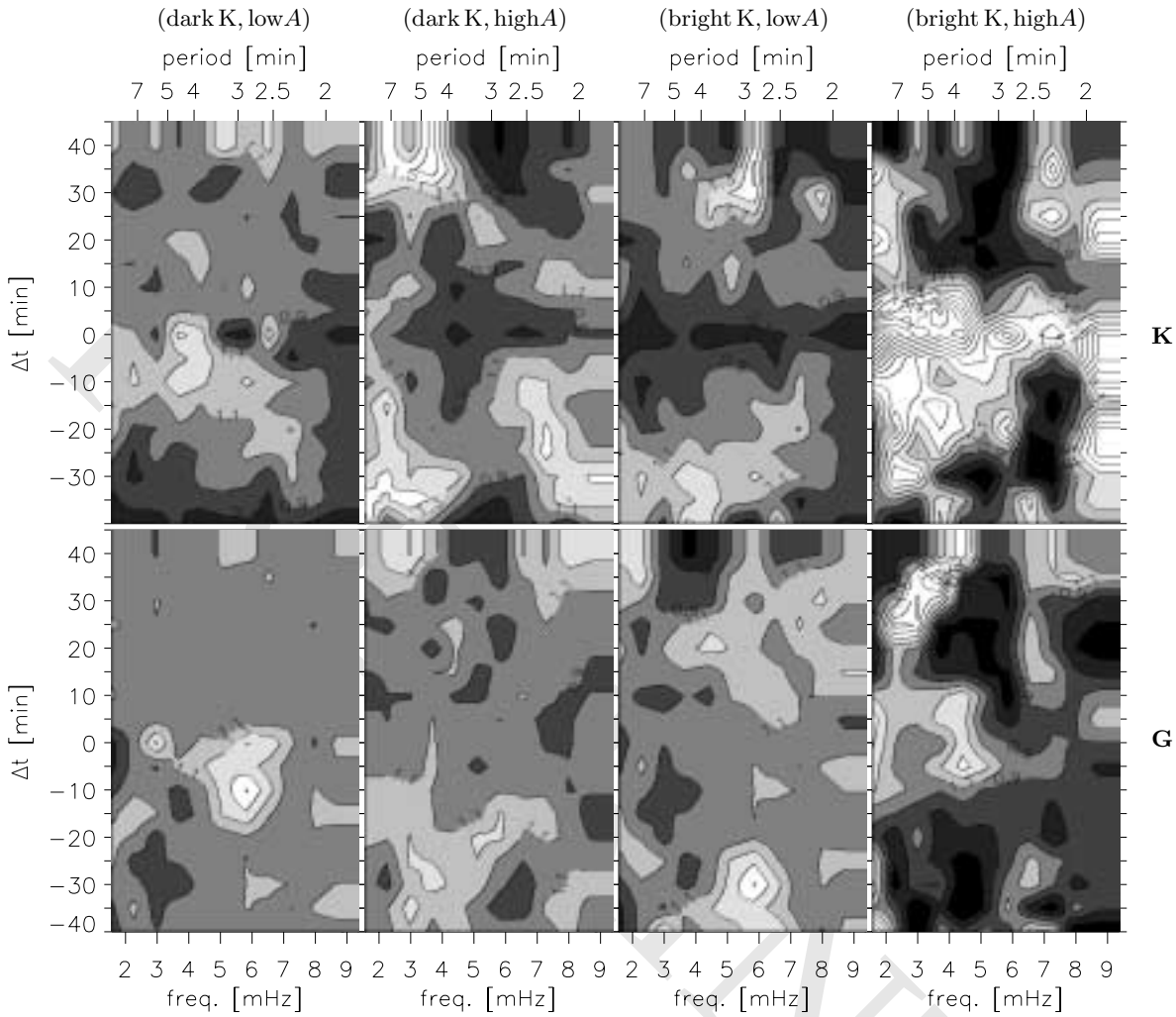

Fig. 6. Time delay charts as in Fig. 5, but the contours now specify the spatial correspondence C between bright pixels or dark pixels in the internetwork parts of the K images and high or low K or G Fourier amplitudes. First column: amount of alignment between dark K pixels and low Fourier amplitude. Second column: dark K pixels and high amplitude. Third column: bright K pixels and low amplitude. Fourth column: bright K pixels and high amplitude. Upper row: K amplitudes (chromosphere). Lower row: G amplitudes (photosphere). Horizontal axes: Fourier frequency (bottom) and periodicity (top). Vertical: time delay Δt, positive when the K pixel is measured as bright or dark after the Fourier amplitude sampling

130%, respectively under 70%, of the average K internetwork brightness in at least 9 of the 18 filtergrams in six-minute intervals at the mid-point of the 22 min data sequences are retained. This procedure produces temporal compatibility with the effective 15-min duration of the Fourier maps and favors K brightness recurrency, i.e., K_{2V} grain "trains", over more temporally isolated events.

The (bright K, high K amplitude) correspondence chart at the upper right displays much structure. The high ridge at $\Delta t = 0$ shows that K_{2V} grain formation is a broad-band phenomenon in wave terms. Its rise to the left corresponds to the tail of persistence over the first 15 min in Fig. 2. The long downward extent of the $C > 1$ area, most notably at 7 min periodicity, indicates that the longer-period waves that contribute to bright K_{2V} grain formation at $\Delta t = 0$ persist over multiple periods.

There are three blobs of high-frequency correspondence along the righthand side of the upper-right chart that we again attribute to seeing jitter. The one at $\Delta t = 0$ illustrates that K_{2V} grains are small. The other two lie at about twenty minutes before and after the K brightness sampling and similarly indicate enhanced probability for the presence of a small bright structure in the chromosphere at the same location. They may illustrate grain recurrency.

The other charts show much less structure. The most significant feature is the extended white ridge at the top of the (bright K, high G amplitude) panel at the lower right, to which we return below.

4. Discussion

Wave excitation. The high peak in the second G panel of Fig. 5 confirms the indication in Fig. 5 of Paper I that dark intergranular lanes tend to show excess waves in the photospheric 2–4 min regime. The large temporal width of the peak, about 20 min, corresponds to the relatively long dark-lane persistence in Fig. 1. In contrast, bright granules do not show alignment with high photospheric wave amplitudes, except for the minor peak at $f = 7$ mHz (lower-right panel of Fig. 5). Thus, local wave excitation does not come from the granules that were taken as pistons in the classical wave generation studies of Evans & Michard (1962), Meyer & Schmidt (1967) and Stix (1970) but rather from persistent intergranular lanes.

The local contribution seems limited to waves in the propagating regime ($f > 5$ mHz); in particular, there are no significant 5-min co-alignment peaks in the G panels of Fig. 5 that might have been expected on the basis of the "acoustical event" studies of Goode et al. (1992), Restaino et al. (1993), Espagnet 1994, Rimmele et al. (1995) and Espagnet et al. (1996). The absence of such 5-min amplitude enhancements at intergranular lanes in Fig. 5 confirms the indication in Paper I that these events are statistically insignificant or that the p-mode pistons should rather be sought below the observable surface as proposed by Brown (1991) and Kumar (1994).

The preferential alignment between 2–4 min waves and dark lanes in the G data does not survive to the chromospheric heights sampled by the K data. This absence of correspondence was interpreted in Paper I as indication of diffraction. Such loss of vertical alignment for propagating waves may also explain the cutoffs near $f > 5$ mHz in various high-correspondence features at large time delay Δt, such as the one at the bottom of the middle (K,K) chart of Fig. 4, near the top of the upper righthand chart in Fig. 5 and near the top in the second K panel of Fig. 6.

Mesoscale migration. There are various features with significant correspondence at large values of Δt, for example the striking peak at $\Delta t = 30$ min in the upper-right panel of Fig. 5. As mentioned above, we suspect that migration of the mesoscale patterning observed in horizontal surface flows plays an important role in these time-delayed alignments. The flows possess pattern difference between divergent areas with a surplus of large bright long-lived granules and convergent areas harboring fewer of these but more dark lanes. Excess sound emission is expected from the mesoscale convergence areas because these are rich in sound-emitting dark lanes (second G panel of Fig. 5) and may also mark the subsurface presence of high-speed downflows ("convective fingers") that may be the principal acoustic sources just below the surface. Since mesoscale patterns evolve and migrate at one-hour time scales (cf. Fig. 3 of Brandt et al. 1994), alignment of high wave amplitude and mesoscale convergence may get replaced at half an hour time delay by alignment to a divergent area containing an overload of bright granules.

In this view, the striking peak in the upper-right panel of Fig. 5 may mark time-lapse co-location between high wave amplitudes and bright granules where the latter have replaced sound-emitting dark lanes or subsurface fingers. The peak value is then high because pixels are averaged over only a few meso cells; averaging over a larger field of view with more variation in mesoscale patterns, flow directions and evolutionary changes would diminish its amplitude. The white blobs near the top and bottom of the fourth G panel in Fig. 5, near the bottom of the 3-min and 2-min (K,K) panels of Fig. 4 and near the top of the fourth G panel of Fig. 6 may be similarly explained. A further speculation along the lines of Paper I is that the 4–5 min location of these delayed features betrays subsurface sources since there is no corresponding 4–5 min non-delayed patch of correspondence in the G panels of Fig. 5.

K_{2V} grain formation. The broad-band ridge of high correspondence in the upper-right panel of Fig. 6 represents a Fourier decomposition of the K_{2V} grain phenomenon and illustrates empirically that grain formation requires a multi-frequency wave mix. It so confirms the split-piston simulations in Fig. 8 of Carlsson & Stein (1997) and the earlier piston experiments of Fleck & Schmitz (1991) and Sutmann & Ulmschneider (1995a, 1995b). Carlsson & Stein employ the observed wave mix at $h = 260$ km to define the piston in their one-dimensional simulations, so that their detailed reproduction of observed H_{2V} grains implies vertical alignment to within the characteristic grain size of 1–2 arcsec over the $h = 260 - 1000$ km height difference. The absence of a similar broad-band ridge in the lower-right G panel indicates that such alignment does not extend to below $h = 260$ km. There is no clear indication of photospheric wave excess that might trigger enhanced K brightness, as proposed for 5-min pistoning by Fleck & Schmitz (1991) and for 3-min pistoning by Cheng & Yi (1996) and Theurer et al. (1997).

On the other hand, the correspondence peak between excess K brightness and intergranular lanes at $\Delta t = 2.5$ min in the upper panel of Fig. 3 suggests preferential alignment between sites of excess 3-min wave excitation (the dark-lane peak in the second G panel of Fig. 5) and K_{2V} grain sites in which the waves need about 2.5 min to propagate up to the Ca II K intensity response height of about 1 Mm where they contribute to bright K_{2V} grain formation in the weak-shock manner computed by Carlsson & Stein. The peak of correspondence with bright granules up to and at $\Delta t = 0$ then implies that such sound-emitting dark sites are followed preferentially by bright granules which persist for some minutes, the reverse of the downflow-driven exploding granules of Rast (1995). The abruptness of such dark-to-bright transitions may also ex-

plain the rather sudden onset of the broad-band ridge in the upper-right panel of Fig. 6. .

Finally, the most significant feature in the G panels of Fig. 6 is the slanted ridge in the lower-right panel for $\Delta t > 20$ min. It indicates that K is preferentially bright above locations that had excess 4–7 min amplitudes 20–40 min earlier in the photosphere. The piston-repeat experiment of Carlsson & Stein (their Fig. 15) shows a delay of about 17 min between photospheric wave behavior and chromospheric H_{2V} response, much longer than the 2–3 min travel time for propagating waves. This delay describes the fact that the state of the overlying chromosphere, in particular its back-fall after preceding shocks, is an important ingredient in K_{2V} grain formation; it takes the piston this length of time to generate the particular shock sequences that produce particular grain behavior. The delay in the fourth G panel of Fig. 6 may portray such response. This may even be the case while mesoscale migration has caused a switch between convergence and divergence (or reversely) over this duration, because the chromospheric response follows the local piston history. Since Carlsson & Stein derived their piston excursions from observations at a fixed location, their simulations sense the actual mesoscale migration across that location in a fashion similar to what we have done here.

5. Conclusion

Our time-delay alignment analyses confirm the striking lack of spatial correspondence between photospheric and chromospheric wave patterning that led us to subsurface wave excitation and wave diffraction in Paper I. In addition, we have found various unexpected alignments at large time delay that seem to be controlled by mesoscale patterning, with the time delay set by pattern migration.

The plots above again demonstrate the complexity in which the photospheric and chromospheric brightness structuring and wave amplitude patterns combine at high spatial and temporal resolution. We regard our various results as indicative for further studies along the same lines, to be pursued with larger and better data sets. It seems particularly worthwhile to employ such alignment analyses to much larger surface samples using photospheric flow tracking to enable studies of chromospheric response to photospheric or subsurface excitation sites while following migrations of the latter over mesoscale and larger distances.

Acknowledgements. N.M. Hoekzema's research was supported by the Netherlands Foundation for Research in Astronomy (NFRA) with financial aid from the Netherlands Organization for Scientific Research (NWO).

References

Brandt P. N., Ferguson S., Shine R. A., Tarbell T. D., Scharmer G. B. 1991, A&A , 241, 219
Brandt P. N., Rutten R. J., Shine R. A., Trujillo Bueno J. 1994, in R. J. Rutten, C. J. Schrijver (eds.), Solar Surface Magnetism, NATO ASI Series C 433, Kluwer, Dordrecht, p. 251
Brown T. M. 1991, ApJ, 371, 396
Carlsson M., Stein R. F. 1997, ApJ , 481, 500
Cheng Q.-Q., Yi Z. 1996, A&A, 313, 971
Cram L. E., Damé L. 1983, ApJ, 272, 355
Espagnet O. 1994, La granulation solaire: origine, pénétration dans la photosphère et interactions avec les oscillations de 5 minutes, Thesis Université Paul Sabatier, Toulouse
Espagnet O., Muller R., Roudier T., Mein P., Mein N., Malherbe J. M. 1996, A&A , 313, 297
Evans J. W., Michard R. 1962, ApJ, 136, 493
Fleck B., Schmitz F. 1991, A&A , 250, 235
Goode P. R., Gough D., Kosovichev A. G. 1992, ApJ , 387, 707
Hoekzema N. M., Rutten R. J., Brandt P. N., Shine R. A. 1997, A&A, in press
Hofmann J., Steffens S., Deubner F. L. 1996, A&A , 308, 192
Kumar P. 1994, ApJ, 428, 827
Lites B. W., Rutten R. J., Kalkofen W. 1993, ApJ, 414, 345
Meyer F., Schmidt H. U. 1967, Zeitschr. f. Astrophys., 65, 274
Muller R., Auffret H., Roudier T., Vigneau J., Simon G. W., Frank Z., Shine R. A., Title A. M. 1992, Nat , 356, 322
November L. J. 1994, Solar Phys. , 154, 1
November L. J., Simon G. W. 1988, ApJ, 333, 427
November L. J., Toomre J., Gebbie K. B., Simon G. W. 1981, ApJ, 245, L123
Rast M. P. 1995, ApJ , 443, 863
Restaino S. R., Stebbins R. T., Goode P. R. 1993, ApJ , 408, L57
Rimmele T. R., Goode P. R., Harold E., Stebbins R. T. 1995, ApJ , 444, L119
Roudier T., Malherbe J. M., November L., Vigneau J., Coupinot G., Lafon M., Muller R. 1997, A&A, 320, 605
Rutten R. J. 1994, in M. Carlsson (ed.), Chromospheric Dynamics, Proc. Miniworkshop, Inst. Theor. Astrophys., Oslo, p. 25
Rutten R. J. 1995, in J. T. Hoeksema, V. Domingo, B. Fleck, B. Battrick (eds.), Helioseismology, Proc. Fourth SOHO Workshop, ESA SP–376 Vol. 1, ESA Publ. Div., ESTEC, Noordwijk, p. 151
Rutten R. J. 1996, in K. G. Strassmeier, J. L. Linsky (eds.), Stellar Surface Structure, Procs. Symp. 176 IAU, Kluwer, Dordrecht, p. 385
Rutten R. J., Uitenbroek H. 1991, Solar Phys., 134, 15
Simon G. W., Title A. M., Topka K. P., Tarbell T. D., Shine R. A., Ferguson S. H., Zirin H., The Soup Team 1988, ApJ, 327, 964
Stix M. 1970, A&A, 4, 189
Sutmann G., Ulmschneider P. 1995a, A&A , 294, 232
Sutmann G., Ulmschneider P. 1995b, A&A , 294, 241
Theurer J., Ulmschneider P., Cuntz M. 1997, A&A, in press
Title A. M., Tarbell T. D., Topka K. P., Ferguson S. H., Shine R. A., the SOUP Team 1989, ApJ, 336, 475
Wang Y., Noyes R. W., Tarbell T. D., Title A. M. 1995, ApJ , 447, 419

This article was processed by the author using Springer-Verlag LaTeX A&A style file *L-AA* version 3.